ChemPubSoc Europe

DOI: 10.1002/chem.201500729

CHEMISTRY A European Journal Full Paper

Lithium-Ion Batteries

Electrochemical Properties of Fiber-in-Tube- and Filled-Structured TiO_2 Nanofiber Anode Materials for Lithium-Ion Batteries

Jung Sang Cho, Young Jun Hong, and Yun Chan Kang*[a]

Abstract: Phase-pure anatase TiO_2 nanofibers with a fiber-in-tube structure were prepared by the electrospinning process. The burning of titanium-oxide-carbon composite nanofibers with a filled structure formed as an intermediate product under an oxygen atmosphere produced carbon-free TiO_2 nanofibers with a fiber-in-tube structure. The sizes of the nanofiber core and hollow nanotube were 140 and 500 nm, respectively. The heat treatment of the electrospun nanofibers at 450 and 500 °C under an air atmosphere produced grey and white filled-structured TiO_2 nanofibers, respectively. The initial discharge capacities of the TiO_2 nanofibers with the fiber-in-tube and filled structures and the commercial TiO_2 nanopowders were 231, 134, and 223 mA h g^{-1}, respectively, and their corresponding charge capacities were 170, 100, and 169 mA h g^{-1}, respectively. The 1000th discharge capacities of the TiO_2 nanofibers with the fiber-in-tube and filled structures and the commercial TiO_2 nanopowders were 177, 64, and 101 mA h g^{-1}, respectively, and their capacity retentions measured from the second cycle were 89, 82, and 52%, respectively. The TiO_2 nanofibers with the fiber-in-tube structure exhibited low charge transfer resistance and structural stability during cycling and better cycling and rate performances than the TiO_2 nanofibers with filled structures and the commercial TiO_2 nanopowders.

Introduction

Nanostructured titanium dioxide (TiO_2) materials have been widely studied for various applications, such as photocatalysis, sensors, solar cells, and energy storage.[1–17] TiO_2 materials have also been studied as anode materials for lithium-ion batteries (LIBs) because of their low density, high abundance, nontoxicity, and structural integrity during repeated cycling.[10–17] Among the various polymorphs of TiO_2, the anatase form with open crystal structure, which originates from the stacking of the zigzag units, can facilitate the intercalation/deintercalation of Li ions.[13–17] However, the Li-ion storage performance of the anatase TiO_2 is also limited by the poor chemical diffusion of lithium. Nanostructured materials with various morphologies, such as nanoparticles, nanorods, nanotubes, and hierarchical nanoporous structure, have been studied to improve the lithium storage properties of the anatase TiO_2 material by shortening the diffusion length of lithium ions.[14–17]

Recently, fiber-in-tube and tube-in-tube materials prepared by the electrospinning process have been studied as electrode materials for energy storage.[18–23] Hong et al. introduced SnO_2 nanofibers with a fiber-in-tube structure prepared by the electrospinning process.[18] Tin-oxide-carbon composite nanofibers with a filled structure formed as an intermediate product were transformed into SnO_2 nanofibers with a fiber-in-tube structure during the heat-treatment process at 500 °C. The unique structure of the SnO_2 nanofibers with a fiber@void@tube configuration improved their electrochemical properties by reducing the diffusion length of the lithium ions and improving the structural stability of the nanotubes during cycling. Li et al. prepared tube-in-tube nanostructured polypyrrole/MnO_2/CNT composites via the in situ chemical oxidation polymerization of pyrrole in the host of an inorganic matrix of MnO_2 and CNTs, with a complex of methyl orange (MO)/$FeCl_3$ used as a reactive self-degraded soft-template.[19] This composite yields good electrochemical reversibility through 1000 cycles in the potential range of −0.6 to 0.4 V. Zhao et al. synthesized a tube-in-tube carbon nanostructure with the MWNTs confined within hollow porous carbon nanotubes and was used to accommodate sulfur.[20] The obtained nanostructure exhibited outstanding electrochemical performance for the cathode. High reversible capacities of 647 mA h g^{-1} remained at 2 A g^{-1} after 200 cycles.

TiO_2 nanofibers with a fiber-in-tube and tube-in-tube structure have been prepared by the electrospinning process.[24,25] Lang et al. prepared solid, hollow, and tube-in-tube porous nanofiber TiO_2 structures with a mixed crystal structure of anatase and rutile phases using a simple non-coaxial electrospinning method from precursor solutions with various concentrations of tetra-*n*-butyl titanate (TBT) used as the Ti component.[24] Chen et al. introduced a multifluidic coaxial electrospinning approach to fabricate the anatase TiO_2 fiber-in-tube structure.[25] However, to the best of our knowledge, the electrochemical properties of the TiO_2 nanofibers with fiber-in-tube

[a] J. S. Cho, Y. J. Hong, Prof. Y. C. Kang
Department of Materials Science and Engineering
Korea University
Anam-Dong, Seongbuk-Gu, Seoul 136-713 (Republic of Korea)
Fax: (+82) 2-928-3584
E-mail: yckang@korea.ac.kr

Supporting information for this article is available on the WWW under http://dx.doi.org/10.1002/chem.201500729.

and tube-in-tube structures as materials for LIBs have not been studied.

In this study, phase-pure anatase TiO_2 nanofibers with a fiber-in-tube structure were prepared using a general electrospinning process. The post-treatment conditions of the electrospun precursor fibers strongly affected the morphologies and crystal structures of the fibers. The burning of titanium oxide-carbon composite nanofibers with filled structure formed as an intermediate product under an oxygen atmosphere produced the anatase TiO_2 nanofibers with a fiber-in-tube structure. A detailed formation mechanism of the anatase TiO_2 nanotube with a fiber-in-tube structure was also proposed. Furthermore, the electrochemical properties of the anatase TiO_2 nanofibers with a fiber-in-tube structure were compared with those of the TiO_2 nanofibers with a filled structure and the mixed crystal structure of the anatase and rutile phases.

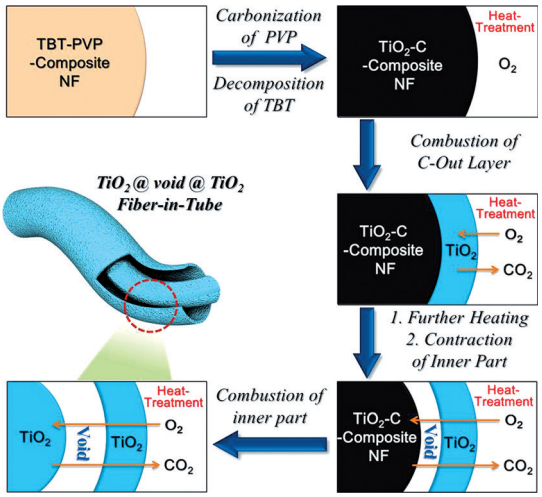

Scheme 1. Formation mechanism of the TiO_2 nanofiber with fiber-in-tube nanostructure from the TBT-PVP composite nanofiber.

Results and Discussion

The formation mechanism of the TiO_2 nanofiber with fiber-in-tube nanostructure from the TBT-PVP composite nanofiber is described in Scheme 1. The TiO_2 fiber-in-tube nanostructure was prepared by a one-pot heat-treatment process of electrospun TBT-PVP composite nanofiber at 450 °C under an oxygen atmosphere. The decomposition of TBT into TiO_2 and carbonization of PVP during the early stage of the heat-treatment process produced the TiO_2-C composite nanofiber with black color. The burning of the TiO_2-C composite nanofiber produced the nanofiber with a core-shell structure of TiO_2-C@TiO_2. Contraction of the TiO_2-C core part by heat evolved by burning of the carbon layer led to the formation of the nanofiber with a yolk-shell structure of TiO_2-C@void@TiO_2. The diffusion of oxygen gas through the TiO_2 shell layer into the void occurred during the second-step burning of the TiO_2-C core to form the TiO_2 nanofiber with fiber-in-tube nanostructure. The burning of the TiO_2-C nanofiber during the short time under oxygen atmosphere was the key requirement to prepare the TiO_2 nanofiber with fiber-in-tube nanostructure.

The morphologies of the nanofibers heat treated at 200 °C under an air atmosphere are shown in Figure 1. The SEM and TEM images in Figure 1a–1c reveal the filled structure. The high-resolution TEM image and inset selected area electron diffraction (SAED) pattern and XRD pattern in Figure 1d and 1e reveal the amorphous-like structure of the nanofibers. The elemental mapping images in Figure 1f reveal the uniform distributions of the Ti, O, and C components all over the nanofiber. The EDX spectrum of the nanofibers heat-treated at 200 °C in Figure S1 reveals the carbonization of PVP into carbon material. The N component originating from the PVP is scarcely observed in the EDX spectrum. The clear nanofiber structure without melting is observed in the TEM image in Figure 1c also reveals the carbonization of PVP during the heating process. Dissolution of PVP did not occur during the sample preparation process for the TEM measurement by dispersing the nanofibers into water. The results of Figure 1 provide evidence of the formation of the TiO_2-C composite nanofiber before the formation of the TiO_2 nanofiber with fiber-in-tube nanostructure.

The morphologies of the nanofibers heat-treated at 450 °C under an oxygen atmosphere are shown in Figure 2. The SEM and TEM images in Figure 2a–2c reveal the formation of a TiO_2 nanofiber with fiber-in-tube nanostructure. A clear void space existing between the nanofiber core and thin shell is observed in the SEM and TEM images. The sizes of the nanofiber core and hollow nanotube measured from the TEM image in Figure 2c are 140 and 500 nm, respectively. The high-resolution TEM image in Figure 2e reveals the clear lattice fringes separated by 0.35 nm, which corresponds to the (101) crystal plane of the anatase TiO_2 phase. The SAED pattern and XRD pattern in Figure 2f and 2g reveal the formation of anatase TiO_2 nanofibers with fiber-in-tube nanostructure by heat treatment at 450 °C under an oxygen atmosphere. The carbon component was not detected in the elemental mapping images of the TiO_2 nanofiber with fiber-in-tube nanostructure, as observed in Figure 2h. Complete combustion of the carbon component by burning resulted in the carbon-free TiO_2 nanofiber with fiber-in-tube nanostructure and white color. This result is further confirmed by TG analysis (Figure S2), in which the weight loss of the TiO_2 nanofiber with fiber-in-tube nanostructure by decomposition of the carbon component was not observed. Based on the XPS spectra (Figure S3), the Ti $2p_{1/2}$ and Ti $2p_{3/2}$ spin-orbital splitting photoelectrons for TiO_2 were located at binding energies of 464.7 and 458.5 eV, respectively, assigned to the presence of typical Ti^{4+}, which are the characteristic peaks of TiO_2.[26,27] The XPS analysis also revealed the carbon-free TiO_2 nanofiber with fiber-in-tube nanostructure. The C 1s spectrum with a peak at approximately 284.6 eV was not observed.

The morphologies of the nanofibers heat-treated at 450 and 500 °C under an air atmosphere are shown in Figure 3. The low- and high-resolution SEM images revealed the formation of the TiO_2 nanofibers with a filled structure irrespective of the heat-treatment temperature under air atmosphere. The heat

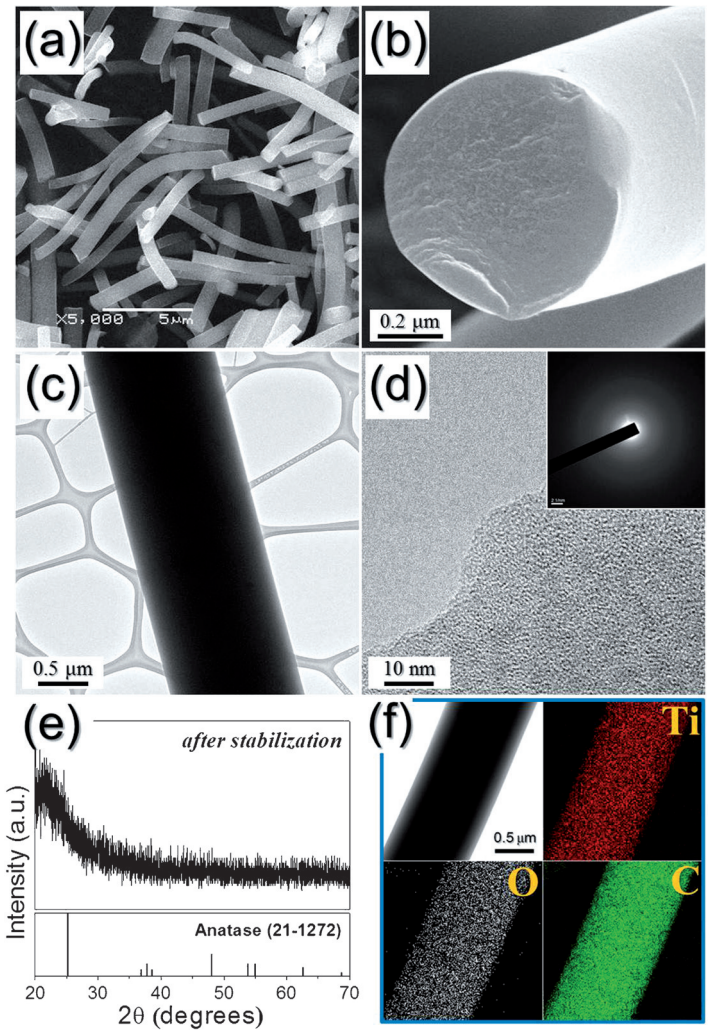

Figure 1. Morphologies, SAED and XRD patterns, and elemental mapping images of the nanofibers heat-treated at 200 °C under an air for 1 h: a) and b) SEM images, c) TEM image, d) HR-TEM image and SAED pattern, e) XRD pattern, and (f) elemental mapping images.

treatment of electrospun TBT-PVP composite nanofibers at 450 and 500 °C under an air atmosphere produced the filled-structured TiO_2 nanofibers with grey and white color, respectively. Slow decomposition of the carbon component without the burning process did not form the TiO_2 nanofiber with fiber-in-tube nanostructure. The nanofibers heat-treated at 450 °C under air atmosphere had anatase TiO_2 phase. On the other hand, the ones heat-treated at 500 °C under an air atmosphere exhibited a mixed crystal structure of the rutile and anatase phase with a ratio of 6:4, as observed in Figure 3d. The carbon-free TiO_2 nanofibers with a filled structure were prepared after heat-treatment at 500 °C under an air atmosphere (Figure S3). The N_2 adsorption-desorption isotherms and Barrett-Joyner-Halenda (BJH) pore size distributions of the three samples are shown in Figure S4. The carbon-free TiO_2 nanofibers with a fiber-in-tube structure contained more well-developed mesopores than those with the filled structure. The BET surface areas of the TiO_2 nanofibers with fiber-in-tube and filled structures and of the commercial TiO_2 nanopowders (P25) were 33, 20, and 56 $m^2 g^{-1}$, respectively.

The electrochemical properties of the anatase TiO_2 nanofibers with fiber-in-tube nanostructure were compared with those of the carbon-free TiO_2 nanofibers with a filled structure and the commercial TiO_2 nanopowders (P25) prepared by the flame method. The SEM image and XRD pattern of P25 are shown in Figure S5. The commercial TiO_2 nanopowders with a mean size of 21 nm exhibited a mixed crystal structure of the anatase and rutile phase (the ratio of anatase to rutile is 8:2). The cyclic voltammogram (CV) curves of the three samples measured in the voltage range of 1.0–3.0 V vs. Li/Li^+ at a scan rate of 0.1 $mV s^{-1}$ are shown in Figure 4a. The anatase TiO_2 nanofibers with fiber-in-tube nanostructure revealed distinct reduction and oxidation peaks at approximately 1.72 and 2.05 V, respectively. The reduction peak was attributed to Li^+ intercalation into the interstitial octahedral site of anatase TiO_2 by the two-phase transition of the structure from tetragonal anatase to orthorhombic $Li_{0.5}TiO_2$ according to the following scheme: $xLi^+ + TiO_2 + xe^- \leftrightarrow Li_xTiO_2$.[28,29] The reduction peaks of the filled-structured TiO_2 nanofibers and TiO_2 nanopowders with a rutile impurity phase are located at a slightly lower potential than that of the anatase TiO_2 nanofibers with fiber-in-tube nanostructure, which revealed that the Li^+ intercalation/deintercalation reactions proceed more easily in the anatase TiO_2 nanofibers with fiber-in-tube nanostructure. The unique structure of TiO_2 nanofibers with fiber-in-tube nanostructure improved the Li-ion diffusion rate. Therefore, Li^+ intercalation reaction could proceed more easily in the TiO_2 nanofibers with fiber-in-tube nanostructure. An extra reduction peak at around 1.35 V was observed in the TiO_2 nanofibers with fiber-in-tube nanostructure. The imperfection of the TiO_2 lattice of fiber-in-tube structure due to low heat temperature of 450 °C during the post-treatment process resulted in the extra reduction peak in the first discharge process.[30] The initial charge and discharge curves of the three samples at a current density of 200 $mA g^{-1}$ are shown in Figure 4b. The commercial TiO_2 nanopowders had clear plateaus at approximately 1.7 and 1.9 V in the initial discharge and charge processes, respectively. However, the TiO_2 nanofibers with fiber-in-tube and filled structures had short plateaus in the initial charge and discharge processes. The different crystallite size of the samples changed the shape of the initial charge and discharge curves.[31–33] The mean crystallite size of the commercial TiO_2 nanopowders for the anatase phase was large as 22 nm. However, the TiO_2 nanofibers with fiber-in-tube and filled structures were low as 14 and 16 nm for the anatase phase, respectively. The initial discharge capacities of the TiO_2 nanofibers with fiber-in-tube and filled structures and of the commercial TiO_2 nanopowders were 231, 134, and 223 $mA h g^{-1}$, respectively, and their corre-

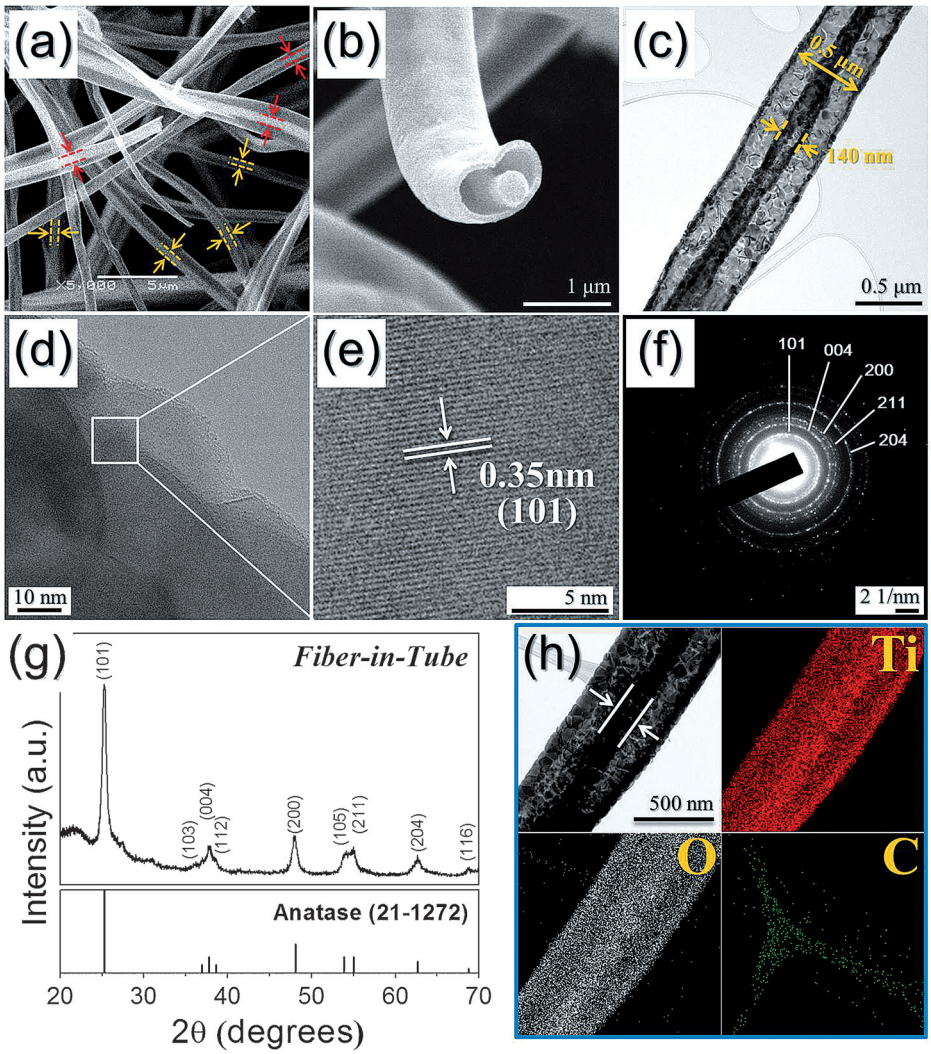

Figure 2. Morphologies, SAED and XRD patterns, and elemental mapping images of the TiO_2 nanofiber with fiber-in-tube nanostructure heat-treated at 450 °C under an oxygen atmosphere: a) and b) SEM images, c) and d) TEM images, e) HR-TEM image, f) SAED pattern, g) XRD pattern, and h) elemental mapping images.

sponding charge capacities were 170, 100, and 169 mA h g^{-1}, respectively. The cycling performances of the three samples at a constant current density of 200 mA g^{-1} are shown in Figure 4c. The 1000th discharge capacities of the TiO_2 nanofibers with fiber-in-tube and filled structures and of the commercial TiO_2 nanopowders were 177, 64, and 101 mA h g^{-1}, respectively, and their capacity retentions measured from the second cycle were 89, 82 and 52%, respectively. The TiO_2 nanofibers with a fiber-in-tube structure maintained their high discharge capacities during the 1000 cycles. The rate performances of the three samples are shown in Figure 4d, with the current density increasing stepwise from 0.2 to 5.0 A g^{-1} and with 10 cycles performed at each step. The TiO_2 nanofibers with a fiber-in-tube structure exhibited better rate performance than the TiO_2 nanofibers with a filled structure and the commercial TiO_2 nanopowders. The final rate capacities of the TiO_2 nanofibers with a fiber-in-tube structure were 167, 132, 111, 94, 84 and 75 mA h g^{-1} at current densities of 0.2, 0.5, 1.0, 2.0, 3.0, and 5.0 A g^{-1}, respectively. The discharge capacity of the TiO_2 nanofibers with a fiber-in-tube structure recovered well to 167 mA h g^{-1} as the current density returned to 0.2 A g^{-1} after 60 cycles.

Electrochemical impedance spectroscopy (EIS) measurements were performed on the TiO_2 nanofibers with fiber-in-tube and filled structures and the commercial TiO_2 nanopowders before and after 100 cycles. The impedance spectra obtained for the three samples before and after cycling are presented in Figure 5a and 5b. The Nyquist plots consist of compressed semicircles in the medium-frequency range, which describe the charge-transfer resistance (R_{ct}) of the electrode.[34,35] The TiO_2 nanofibers with fiber-in-tube structures exhibited low charge-transfer resistances compared with the nanofibers with a filled structure and the commercial TiO_2 nanopowders before and after cycling. The TiO_2 nanofibers with a fiber-in-tube structure had low charge-transfer resistance even after 100th cycling. However, the structural destruction of the TiO_2 nanofibers with a filled structure and the commercial TiO_2 nanopowders increased the charge transfer resistance after cycling. Therefore, the TiO_2 nanofibers with a fiber-in-tube structure exhibiting low charge transfer resistance and structural stability during cycling had higher capacities than the TiO_2 nanofibers with a filled structure. The morphologies of the TiO_2 nanofibers with fiber-in-tube and filled structures obtained after 1000 cycles are shown in Figure S7. The TiO_2 nanofibers with fiber-in-tube structure maintained their morphology even after repeated lithium insertion and desertion processes as shown by SEM image. However, the TiO_2 nanofiber with filled structure was broken into several pieces after cycling.

Conclusion

In this study, TiO_2 nanofibers with fiber-in-tube and filled structures were prepared by post-treatment of electrospun TBT-PVP composite nanofibers under oxygen and air atmospheres, respectively. The burning of TiO_2-C nanofibers during a short time under an oxygen atmosphere was the key requirement to prepare the TiO_2 nanofibers with a fiber-in-tube nanostructure.

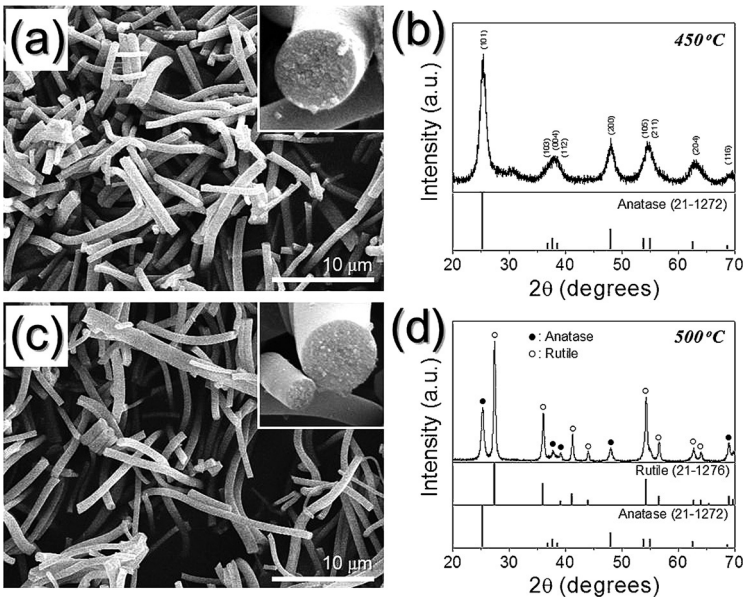

Figure 3. Morphologies and XRD patterns of the TiO_2 nanofibers with filled structure: a) and b) TiO_2 nanofibers heat-treated at 450 °C under air atmosphere, c) and d) TiO_2 nanofibers heat-treated at 500 °C under air atmosphere.

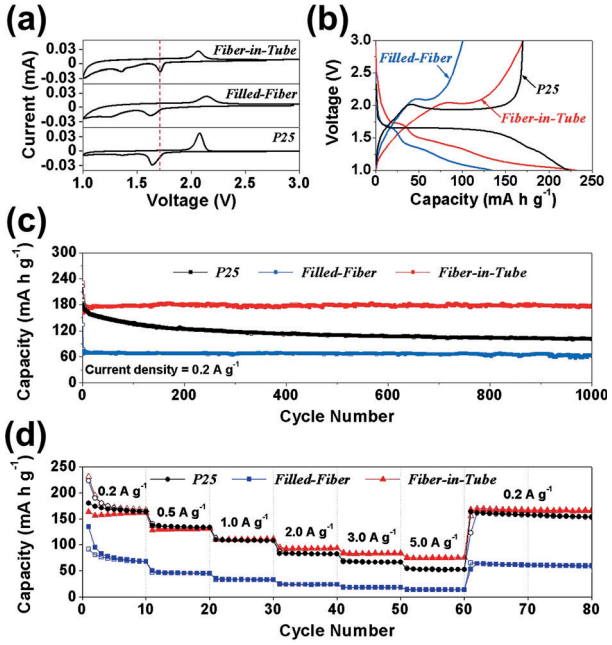

Figure 4. Electrochemical properties of the TiO_2 nanofibers with fiber-in-tube structure and TiO_2 nanofibers with a filled structure and the commercial TiO_2 nanopowders (P25): a) CV curves, b) initial charge-discharge curves, c) cycling performances, and d) rate performances.

The repeated combustion and contraction of the electrospun nanofibers led to the formation TiO_2 nanofibers with a TiO_2@void@TiO_2 structure through TiO_2-C and TiO_2-C@void@-TiO_2 nanofibers. The anatase TiO_2 nanofibers with a fiber-in-tube structure exhibited superior Li-ion storage properties compared with the TiO_2 nanofibers with a filled structure and commercial TiO_2 nanopowders.

Experimental Section

Sample preparation: Precursor composite fibers composed of TBT ($C_{16}H_{36}O_4Ti$) and polyvinylpyrrolidone (PVP, M_w: 58000) were prepared by electrospinning. In a typical procedure, 30 wt% of PVP was dissolved in a solution containing 40 mL of ethanol and 4 mL of acetic acid with stirring and ultrasonication to obtain a transparent homogeneous solution. Then, 20 wt% of TBT was added to this solution. The mixed solution was then loaded into a plastic syringe and electrospun with a stainless steel needle (25 gauge) at a flow rate of 20 mL h^{-1} and an applied voltage of 25 kV over a collection distance of 15 cm. The electrospun fibers were collected on an aluminum foil and were immediately transferred to a vacuum drying oven maintained at 60 °C to reduce the hygroscopicity. The dried electrospun fibers were heat treated at 450 and 500 °C for 5 h under oxygen and air atmospheres, respectively. The rate of increase in the reactor temperature was 5 °C min^{-1}.

Characterization: The microstructures of the nanofibers were examined by field-emission scanning electron microscopy (FE-SEM, S-4800, Hitachi) and field-emission transmission electron microscopy (FE-TEM, JEM-2100F, JEOL). In addition, their crystal phases were evaluated by X-ray diffractometry (XRD, X'Pert PRO MPD) using

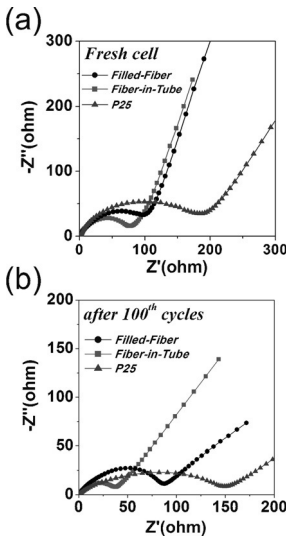

Figure 5. Electrochemical impedance spectroscopy (EIS) of the TiO_2 nanofibers with fiber-in-tube and filled structures and the commercial TiO_2 nanopowders (P25): a) Nyquist impedance plots before cycling and b) Nyquist impedance plots after 100th cycling.

$Cu_{K\alpha}$ radiation ($\lambda = 1.5418$ Å) at the Korea Basic Science Institute (Daegu). The phase ratio between anatase and rutile in the structures were identified using the TOPAS program based on the Rietveld refinement. X-ray photoelectron spectroscopy (XPS, Thermo Scientific K-Alpha) with a focused monochromatic $Al_{K\alpha}$ at 12 kV and 20 mA was used to analyze the composition of the specimens. The surface areas of the nanofibers were measured using the Brunauer-Emmett-Teller (BET) method using N_2 as the adsorbate gas. Thermogravimetric analysis was performed using a Pyris 1 TGA (Perkin-Elmer) within a temperature range of 25–650 °C at a heating rate of 10 °C min^{-1} under a static air atmosphere. The compositions of

the nanofibers were analyzed by energy dispersive X-ray (EDX) detectors at an accelerating voltage of 200 kV.

Electrochemical measurements: The capacities and cycle properties of the TiO_2 nanofibers with fiber-in-tube and filled structures were measured using 2032-type coin cells. The cell electrodes were prepared using a slurry consisting of 70 wt% active anode material, 20 wt% carbon black (Super-P) as a conductive material, and 10 wt% binder composed of sodium carboxymethyl cellulose (CMC) on a copper foil. Lithium metal and a microporous polypropylene film were used as the counter electrode and separator, respectively. The electrolyte was created by dissolving 1 M $LiPF_6$ in a mixture of fluoroethylene carbonate and dimethyl carbonate (FEC/DMC, 1:1 v/v). The entire cell was assembled in an argon atmosphere in a glove box. The charge/discharge characteristics of the samples were measured at various current densities in the voltage range of 1.0–3.0 V. Cyclic voltammetry measurements were performed at a scan rate of 0.1 mV s^{-1} between 1.0 and 3.0 V. Electrochemical impedance spectra of the TiO_2 nanofibers with fiber-in-tube and filled structures were analyzed in the frequency range between 0.1 Hz and 1 MHz at room temperature with a signal amplitude of 5 mV.

Acknowledgements

This work was supported by the Energy Efficiency & Resources Core Technology Program of the Korea Institute of Energy Technology Evaluation and Planning (KETEP), granted financial resource from the Ministry of Trade, Industry & Energy, Republic of Korea (201320200000420).

Keywords: energy storage materials · lithium · nanostructures · synthesis design · titanium dioxide

[1] K. P. Zanoni, R. C. Amaral, N. Y. Murakami Iha, *ACS Appl. Mater. Interfaces* **2014**, *6*, 10421 – 10428.
[2] J. Yu, J. Low, W. Xiao, P. Zhou, M. Jaroniec, *J. Am. Chem. Soc.* **2014**, *136*, 8839 – 8842.
[3] J. Villanueva-Cab, S. R. Jang, A. F. Halverson, K. Zhu, A. J. Frank, *Nano Lett.* **2014**, *14*, 2305 – 2309.
[4] T. Tachikawa, S. Yamashita, T. Majima, *J. Am. Chem. Soc.* **2011**, *133*, 7197 – 7204.
[5] H. Song, K. Jo, B. Y. Jung, G. Y. Jung, *Nano Res.* **2014**, *7*, 104 – 109.
[6] G. D. Moon, J. B. Joo, M. Dahl, H. Jung, Y. Yin, *Adv. Funct. Mater.* **2014**, *24*, 848 – 856.
[7] V. Roiati, E. Mosconi, A. Listorti, S. Colella, G. Gigli, F. De Angelis, *Nano Lett.* **2014**, *14*, 2168 – 2174.
[8] P. Da, W. Li, X. Lin, Y. Wang, J. Tang, G. Zheng, *Anal. Chem.* **2014**, *86*, 6633 – 6639.
[9] A. K. Chandiran, A. Yella, M. T. Mayer, P. Gao, M. K. Nazeeruddin, M. Grätzel, *Adv. Mater.* **2014**, *26*, 4309 – 4312.
[10] M. Pfanzelt, P. Kubiak, M. Fleischhammer, M. Wohlfahrt-Mehrens, *J. Power Sources* **2011**, *196*, 6815 – 6821.
[11] N. Takami, Y. Harada, T. Iwasaki, K. Hoshina, Y. Yoshida, *J. Power Sources* **2015**, *273*, 923 – 930.
[12] S. J. Kim, S. Y. Noh, A. Kargar, D. Wang, G. W. Graham, X. Pan, *Chem. Commun.* **2014**, *50*, 9932 – 9935.
[13] H. Ren, R. Yu, J. Wang, Q. Jin, M. Yang, D. Mao, D. Kisailus, H. Zhao, D. Wang, *Nano Lett.* **2014**, *14*, 6679 – 6684.
[14] Z. Lin, M. Zheng, B. Zhao, G. Wang, L. Pu, Y. Shi, *J. Solid State Electrochem.* **2014**, *18*, 1673 – 1681.
[15] M. Sanad, M. Rashad, K. Powers, *Appl. Phys. A* **2015**, *118*, 665 – 674.
[16] G. Zhang, H. B. Wu, T. Song, U. Paik, X. W. Lou, *Angew. Chem. Int. Ed.* **2014**, *53*, 12590 – 12593; *Angew. Chem.* **2014**, *126*, 12798 – 12801.
[17] J. Sundaramurthy, V. Aravindan, P. Suresh Kumar, S. Madhavi, S. Ramakrishna, *J. Phys. Chem. C* **2014**, *118*, 16776 – 16781.
[18] Y. J. Hong, J. W. Yoon, J. H. Lee, Y. C. Kang, *Chem. Eur. J.* **2015**, *21*, 371 – 376.
[19] J. Li, T. Que, J. Huang, *Mater. Res. Bull.* **2013**, *48*, 747 – 751.
[20] Y. Zhao, W. Wu, J. Li, Z. Xu, L. Guan, *Adv. Mater.* **2014**, *26*, 5113 – 5118.
[21] S. Peng, L. Li, Y. Hu, M. Srinivasan, F. Cheng, J. Chen, S. Ramakrishna, *ACS Nano* **2015**, *9*, 1945 – 1954.
[22] Z. Cai, L. Xu, M. Yan, C. Han, L. He, K. M. Hercule, C. Niu, Z. Yuan, W. Xu, L. Qu, *Nano Lett.* **2015**, *15*, 738 – 744.
[23] M. Yan, F. Wang, C. Han, X. Ma, X. Xu, Q. An, L. Xu, C. Niu, Y. Zhao, X. Tian, *J. Am. Chem. Soc.* **2013**, *135*, 18176 – 18182.
[24] L. Lang, D. Wu, Z. Xu, *Chem. Eur. J.* **2012**, *18*, 10661 – 10668.
[25] H. Chen, N. Wang, J. Di, Y. Zhao, Y. Song, L. Jiang, *Langmuir* **2010**, *26*, 11291 – 11296.
[26] K. H. Choi, N. Duraisamy, N. M. Muhammad, I. Kim, H. Choi, J. Jo, *Appl. Phys. A* **2012**, *107*, 715 – 722.
[27] T. Mariyappan, J. Y. Kim, Y. Ko, H. J. Song, H. Shin, J. Song, Y. Lee, M. Natarajan, D. Velauthapillai, C. Lee, *Nanoscale* **2014**, *6*, 8585 – 8589.
[28] B. J. Morgan, P. A. Madden, *Phys. Rev. B* **2012**, *86*, 035147.
[29] I. Moriguchi, R. Hidaka, H. Yamada, T. Kudo, H. Murakami, N. Nakashima, *Adv. Mater.* **2006**, *18*, 69 – 73.
[30] Z. Wang, J. Sha, E. Liu, C. He, C. Shi, J. Li, N. Zhao, *J. Mater. Chem. A* **2014**, *2*, 8893 – 8901.
[31] Y. Xu, G. Jian, Y. Liu, Y. Zhu, M. R. Zachariah, C. Wang, *Nano Energy* **2014**, *3*, 26 – 35.
[32] Y. Yin, Y. Hu, P. Wu, H. Zhang, C. Cai, *Chem. Commun.* **2012**, *48*, 2137 – 2139.
[33] Y. Liu, Y. Xu, X. Han, C. Pellegrinelli, Y. Zhu, H. Zhu, J. Wan, A. C. Chung, O. Vaaland, C. Wang, *Nano Lett.* **2012**, *12*, 5664 – 5668.
[34] B. Guo, X. Wang, P. F. Fulvio, M. Chi, S. M. Mahurin, X. G. Sun, S. Dai, *Adv. Mater.* **2011**, *23*, 4661 – 4666.
[35] Y. N. Ko, S. B. Park, K. Y. Jung, Y. C. Kang, *Nano Lett.* **2013**, *13*, 5462 – 5466.

Received: February 21, 2015
Published online on June 26, 2015

